Abnormal orderly transformation in supercooled state of an Al-based alloy

Jiajia Han,[1,*] Cuiping Wang,[1] Shuiyuan Yang,[1] Yong Lu,[1] and Xingjun Liu[1,2,3,†]

[1]*College of Materials and Fujian Provincial Key Laboratory of Materials Genome, Xiamen University, Xiamen 361005, People's Republic of China*

[2]*State Key Laboratory of Advanced Welding and Joining, Harbin Institute of Technology, Harbin 150001, People's Republic of China*

[3]*Institute of Materials Genome and Big Data, Harbin Institute of Technology, Shenzhen 518055, People's Republic of China*

(Received 31 March 2020; revised 31 July 2020; accepted 15 September 2020; published 28 September 2020)

To understand the underlying mechanism behind the precipitation of high-density face-centered cubic Al nanoparticles during the annealing or preparation of Al-based metallic glass, we used molecular dynamics simulation technique to study the atomic structure evolution of Al-rich and Al-depleted melts in the Al-Zr binary system under rapid cooling conditions. From the quantitative characterization of thermodynamic properties, kinetic properties, and atomic structure, we found that an abnormal orderly transformation occurs in the supercooled liquid of Al-rich alloy, which includes two basic stages, namely, directional diffusion and stabilization of defect clusters. The thermodynamic essence of this transformation is to reduce the Gibbs free energy of the entire system by improve the cluster packing efficiency of atomic structure, preventing the supercooled liquid from being in an unstable state. An important consequence of the abnormal orderly transformation is the formation of nanoscale Al-rich regions in the supercooled liquid. These regions can readily promote the precipitation of high-density face-centered cubic Al nanoparticles, thereby reducing the complete amorphization ability of Al-based alloy melt.

DOI: 10.1103/PhysRevMaterials.4.093608

I. INTRODUCTION

A long-term challenge for Al-based metallic glass (MG) is that its glass-forming ability (GFA) is very poor compared to other family systems [1,2]. Over the past two or three decades, materials scientists and physicists have dedicated themselves to addressing this, arguably one of the most disturbing issues in the field of MG, but they have never been able to get full understanding of the underlying mechanism. Lacking a complete perspective of this problem makes it impossible for us to break the size limit, and Al-based MG can be mostly obtained in thin ribbons [3–8]. This makes Al-based MG, one of the most promising new metal materials in engineering applications [9–12], unable to give full potential to its advantages of light weight and high strength [9,13–16].

Al-based MGs have several peculiar features that distinguish it from other systems. For instance, the best glass-forming compositions are far off eutectic points for the binary and ternary Al-based alloys that have been studied so far, and the GFA is very sensitive to the alloy composition [17–20]. The composition of Al-based MG significantly deviates from the Al-rich side although their compositional feature meet the atomic size criteria employed for producing bulk MGs [21]. In addition, the minor addition of alloy elements to improve GFA has little effect on most Al-based MGs [22–24] and not all Al-based MGs have a discernible glass transition signal [25–27]. A large number of studies have manifested that the currently available knowledge cannot readily understand the GFA of Al-based alloy systems [16,28–32], and the previous structural models and empirical criteria for characterizing ordinary MGs do not always work well for Al-based MGs [33–36], which gives rise to difficulty in exploring Al-based bulk metallic glass (BMG) with enhanced GFA.

Rapidly quenched Al-based MGs are usually characterized by a primary crystallization reaction either annealing the as-quenched Al-based amorphous alloys [27,37–40] or by the direct solidification of the molten alloy at a cooling rate lower than the critical cooling rate [41,42], which produces a high density of face-centered cubic (FCC) Al nanocrystals dispersed in the amorphous matrix. The intermetallic phases were, nevertheless, frequently precipitated as the second phase, regardless of the thermodynamic driving free energy for crystallization favors the Al-rich intermetallic phase over the FCC-Al within the hypereutectic glass-forming composition range [43]. It has been suggested that the supercooled liquid of Al-based alloy may undergo phase separation, contributing to the subsequent heterogeneous nucleation of the FCC-Al at the interfaces between the phase separating regions [44–46]. Others also argue that there already exists pre-existing FCC-Al nuclei or medium range order in the as-quenched glassy matrix, which simply grow during annealing [38,47,48]. These are related to the two most popular models commonly used to discuss the experimental phenomena, namely, "phase separation" and "quenched-in nuclei."

The reason why the poor GFA of Al-based MG has not been overcome until now is that both models only give the apparent description of the experimental phenomena, and do not well answer many essential questions, such as the origin of phase separation in supercooled liquid, how the phase

*jiajiahan@xmu.edu.cn
†xjliu@hit.edu.cn

separation is related to a high nucleation rate, whether nanoscale phase separation is common in Al-based glasses and so on [45,49,50]. Finding the underlying mechanism to explain the key experimental observations not only contributes to the development of the novel amorphous/nanocrystal products, but also plays an important role in revealing the glass formation and developing the manufacturing process of Al-based MG [51,52].

Given the phenomena observed from a large number of experiments, we speculate that some sort of abnormal orderly transformation (AOT) may occur in Al-based alloy during rapid cooling. The aim of this work is to reveal the physical nature behind the experimental phenomena and quantitatively describe the special behavior of Al-based alloys in the supercooled liquid state. Here, we take the typical Al-Zr binary system as a case study, in which four compounds were designated covering the compositions from Al-depleted to Al-rich sides. In the Al-rich side, Al_3Zr compound was deliberately chosen, by considering that the Al content is typically lower than that in the current Al-based MGs and the thermodynamically favored phase is a compound rather than a solid solution. Using this approach can largely avoid the peculiarity of case study, and the conclusions drawn would be more universal.

II. METHODS

Classical molecular dynamics simulations are performed using a large-scale atomic/molecular massively parallel ssimulator (LAMMPS) [53]. To accurately describe the interatomic interactions for both crystalline and amorphous states in the Al-Zr system, the newly developed embedded atom method (EAM) type of Al-Zr interatomic potential developed by Sheng [54] was employed, which was obtained by fitting the potential energy surface calculated by *ab initio* of over 600 configurations, including crystalline phases, liquids and MGs for several crucial structures respectively of Al_3Zr, Al_2Zr, AlZr, Al_3Zr_4, Al_3Zr_5, $AlZr_2$, and $AlZr_3$ compounds. It has been carefully validated extensively by comparing *ab initio* calculations with experimental data, and used to study atomic structure of supercooled liquid and MGs [55,56]. The simulations were performed on systems consisted of 12 168 atoms for $AlZr_3$, 10 976 atoms for Al_3Zr_5, 12 348 atoms for Al_4Zr_5, and 10 816 atoms for Al_3Zr, respectively, by using an isothermal-isobaric (NPT) ensemble and periodic boundary condition in all three directions. In the calculations of liquid-crystal coexistence model, the number of atoms is doubled. The time step Δt is chosen as 2 fs ($1\,\mathrm{fs} = 10^{-15}\,\mathrm{s}$), which was proved to be small enough to achieve the convergence of potential energy and characteristic structure. Two kinds of simulation processes are designed respectively, namely, continue cooling and periodic cooling.

In the simulation of continue cooling, each system is heated up to 2000 K (much higher than melting point) and run 1×10^6 timesteps to reach equilibrium, followed by the cooling process at cooling rates of $8.5 \times 10^{10}\,\mathrm{K\,s^{-1}}$, $4.25 \times 10^{10}\,\mathrm{K\,s^{-1}}$, and $8.5 \times 10^{9}\,\mathrm{K\,s^{-1}}$. In parallel to continue cooling, a quench strategy that simulation time increase linearly close to glass transition temperature (T_g) was employed to sampling trajectory for the calculation of thermodynamic and kinetic properties from 2000 to 300 K. This takes places in many discrete steps, which each contain a ramped temperature change from the last step and then a hold at a constant temperature. The average cooling rate is $5 \times 10^{10}\,\mathrm{K\,s^{-1}}$, and the relaxation time for each temperature is from 1 ns to 10 ns, depending on the specific temperature. The last 2000 configurations are collected in each of certain sampling points for kinetics analysis, and 2000 configurations by every step are used for other analyses.

By constructing a two-phase model composed of crystal and liquid with the same composition, it is possible to study the evolution of the atomic structure of the supercooled liquid under a stable crystal potential field, such as the growth of crystal grains. The initial solid-liquid configurations are constructed by conjoining the stable crystal along the in-plane direction (001) and the liquid at their common cross-sections. The long direction of the cell was chosen to be normal to the solid-liquid interface and the in-plane dimensions were fixed to have periodic lengths dictated by the equilibrium lattice constant (at zero pressure) for the crystal. After the perfect crystal cell was constructed, NPT ensemble dynamics was used to melt the atoms in the range of three-quarter length perpendicular to the interface at 2000 K. Subsequently, the mixture of melt and frozen crystal with two interfaces was cooled down continually to 300 K, during which the length of the crystal was allowed to change to maintain zero normal pressure.

To evaluate the relative growth rate of different crystals on rapid cooling, the bond orientational order (BOO) parameter developed by Steinhardt *et al.* [57] is introduced, which is widely used to characterize the bond orientational symmetry surrounding the specific atom [58]. The local structure of particle i is characterized by the BOO parameters defined as follows:

$$Q_l(i) = \sqrt{\frac{4\pi}{2l+1}\sum_{m=-1}^{l}|Q_{lm}(i)|^2}, \tag{1}$$

$$W_l = \frac{\sum_{\substack{m1,m2,m3 \\ m1+m2+m3=0}} \begin{bmatrix} l & l & l \\ m_1 & m_2 & m_3 \end{bmatrix} Q_{lm1}Q_{lm2}Q_{lm3}}{\sum_{m=-l}^{l}|Q_{lm}(i)|^2}, \tag{2}$$

where

$$Q_{lm}(i) = \frac{1}{n(i)}\sum_{j=1}^{n(i)} Y_{lm}(r_{ij}), \tag{3}$$

where, $n(i)$ is the coordination number of particle i. $Y_{lm}(r_{ij})$ are spherical harmonics, where r_{ij} represents a vector from particle i to j, l is an integer, and m goes from $-l$ to $+l$. In general, BOO has good resolution only for the crystalline and amorphous phases of a close-packed structure [59]. We found that except for $AlZr_3$, the BOO values of the compounds cover a wide range, which easily overlaps with the BOO values of the amorphous structure. To this end, we distinguish between amorphous and crystalline structures by adjusting the combined values of w_4 and w_6 in the BOO parameters.

As a key transport property, the shear viscosity describes the macroscopic liquid state dynamics, and can be calculated

by using the appropriate Green-Kubo (GK) relation [60]:

$$\eta = \frac{V}{k_B T}\int_0^\infty dt\,\langle\sigma_{xy}(0)\sigma_{xy}(t)\rangle, \tag{4}$$

where σ_{xy} is the off-diagonal x-y component of the stress tensor, k_B is the Boltzmann constant, T is the absolute temperature of the system, and V is the volume of the metallic liquid system. In the present work, the shear viscosity was calculated at temperatures above T_g by ~100 K from the simulated data obtained during the cooling process under a cooling rate of 5×10^{10} K s^{-1}, and was fitted using the Vogel-Fulcher-Tamman (VFT) relationship [61],

$$\eta(T) = \eta_0^{\mathrm{VFT}} \exp\left(\frac{B}{T - T_0}\right), \tag{5}$$

where η_0^{VFT}, B, and the Vogel temperature T_0 are fitting parameters. The resultant fragility is determined by fitting according to the following expression:

$$m = \left.\frac{d(\log\eta)}{d\left(\frac{T_g}{T}\right)}\right|_{T=T_g}. \tag{6}$$

Note that T_g here is a rheological definition based on a glass transition temperature of a viscosity equal to 10^{12} Pa s, whose value is generally consistent with the calorimetric T_g extracted from the curve of temperature-dependent physical properties.

Considering that the composition of these alloys corresponds to a single compound with the highest thermodynamic stability, the Gibbs free energy of the corresponding compound is then regarded as a reference state to evaluate the thermodynamic driving force to transform the supercooled liquid into the stable compound, which is defined as $\Delta G = G^{\mathrm{l}} - G^{\mathrm{c}}$. Here, G^{l} is the Gibbs free energy of liquid in the stable or metastable state, and G^{c} is the Gibbs free energy of crystalline phase that is stable or metastable under random equilibrium fluctuations at the given temperature and pressure. The magnitude of ΔG determines the thermodynamic nature of crystal nucleation and growth. Gibbs free energy combines enthalpy and entropy into a single value: $G = H - TS$, where H is enthalpy and S is entropy of a certain system. The value of H can be directly obtained from MD simulation. For a metallic system, the integral entropy S^{total} of alloys can be defined as

$$S^{\mathrm{total}} = S^{\mathrm{total}} + S^{\mathrm{ele}} + S^{\mathrm{conf}}, \tag{7}$$

where S^{vib} is the vibrational entropy, S^{ele} is the electronic entropy, and S^{conf} is the configurational entropy. The S^{vib} is calculated from two-phase thermodynamic (2PT) model [62,63], in which the anharmonic effects in liquid are treated by dividing the density of state distribution of component i, $D_i^{\mathrm{l}}(v)$, into solid-like $D_i^{\mathrm{s}}(v)$ and gas-like components $D_i^{\mathrm{g}}(v)$ as a function of vibrational frequency v. The S^{con} of nonideal system can be obtained by considering the chemical environment around different types of atoms [64]:

$$s^{\mathrm{conf}} = \frac{k_B}{\sum_{i=1}^m Z_i c_i}\sum_{j,k=1}^m\left[Z_j c_j f_{jk}\ln\left(\frac{\sum_{l=1}^m Z_l c_l f_{lk}}{Z_j c_j f_{jk}}\right)\right], \tag{8}$$

where the upper bound of each summation m depends on the component number, Z_i represents the coordination number of ith atom, f_{ij} is the fraction of coordination number of ith atom with respect to jth atom, and c_i is the concentration of i species. In the present work, the contribution of S^{ele} to S^{total} is ignored, because the values of S^{ele} in the crystal and liquid states are close at a certain temperature and will cancel each other out in the calculation.

To discuss topological and chemical ordering in the current binary system, Bhatia-Thornton formalism is introduced. Three partial pair-distribution functions (PDFs), namely, g_{NN}, g_{NC}, and g_{CC}, are, respectively, calculated for these four alloys in various states. The definition is shown as follows [65]:

$$g_{\mathrm{NN}} = c_{\mathrm{Al}}^2 g_{\mathrm{AlAl}}(r) + c_{\mathrm{Zr}}^2 g_{\mathrm{ZrZr}}(r) + 2c_{\mathrm{Al}}c_{\mathrm{Zr}}g_{\mathrm{AlZr}}(r), \tag{9}$$

$$g_{\mathrm{CC}}(r) = c_{\mathrm{Al}}c_{\mathrm{Zr}}[g_{\mathrm{AlAl}}(r) + g_{\mathrm{ZrZr}}(r) - 2g_{\mathrm{AlZr}}(r)], \tag{10}$$

$$g_{\mathrm{NC}}(r) = c_{\mathrm{Al}}[g_{\mathrm{AlAl}}(r) - g_{\mathrm{AlZr}}(r)] - c_{\mathrm{Zr}}[g_{\mathrm{ZrZr}}(r) - g_{\mathrm{AlZr}}(r)], \tag{11}$$

where c_{Al} and c_{Zr} represent the atomic fraction of Al and Zr, respectively.

The general expression for the overall rate of crystal growth can be written as [66]

$$v(T) = \frac{CLD_{\mathrm{eff}}(T)}{\sigma^2}\left[1 - \exp\left(\frac{-\Delta G(T)}{RT}\right)\right], \tag{12}$$

where $\Delta G(T)$ is the bulk energy difference between the liquid and crystal, R is the gas constant, and L is the lattice spacing normal to the surface, which is 2.19 Å, 1.36 Å, 2.81 Å, and 1.99 Å for $AlZr_3$, Al_3Zr_5, Al_4Zr_5, and Al_3Zr, respectively. σ is a reference particle diameter, determined by the position of the first peak in the $g_{\mathrm{NN}}(r)$. C is a constant related to the structural and compositional difference between crystal and supercooled liquid. According to the results of coordination number (CN) and $g_{\mathrm{NN}}(r)$, 2 and 1.5 are applied to $AlZr_3$ and Al_3Zr, respectively, and 1 is set for both Al_3Zr_5 and Al_4Zr_5. $D_{\mathrm{eff}}(T)$ is effective diffusion coefficient, calculated through the equation as follows [67]:

$$D_{\mathrm{eff}} = \frac{1}{\sum_i \frac{v_i^2}{x_i D_i}}, \tag{13}$$

where D_i represents D_{Al} or D_{Zr}, x_i is the molar fraction of Al or Zr, and the parameter v_i is the coefficient describing the stoichiometric composition of the crystalline phase.

III. RESULTS

A. Structural transition in the supercooled liquid

Figure 1(a) and Fig. S1 of the Supplemental Material [68] show the potential energy (PE) of $AlZr_3$, Al_3Zr_5, Al_4Zr_5, and Al_3Zr compounds as a function of temperature upon continued cooling. The cooling rates of 8.5×10^{10} K s^{-1}, 4.25×10^{10} K s^{-1}, and 8.5×10^9 K s^{-1} were applied from 2000 to 300 K. Glass transition is characterized by the crossover on the PE curve. Whether or not there is orderly behavior can be examined by the abrupt change in PE. From Fig. S1 of the Supplemental Material [68], the $AlZr_3$, Al_3Zr_5, and Al_4Zr_5 compounds do not exhibit appreciable orderly behavior at given cooling rates. The slight reduction in PE by slower

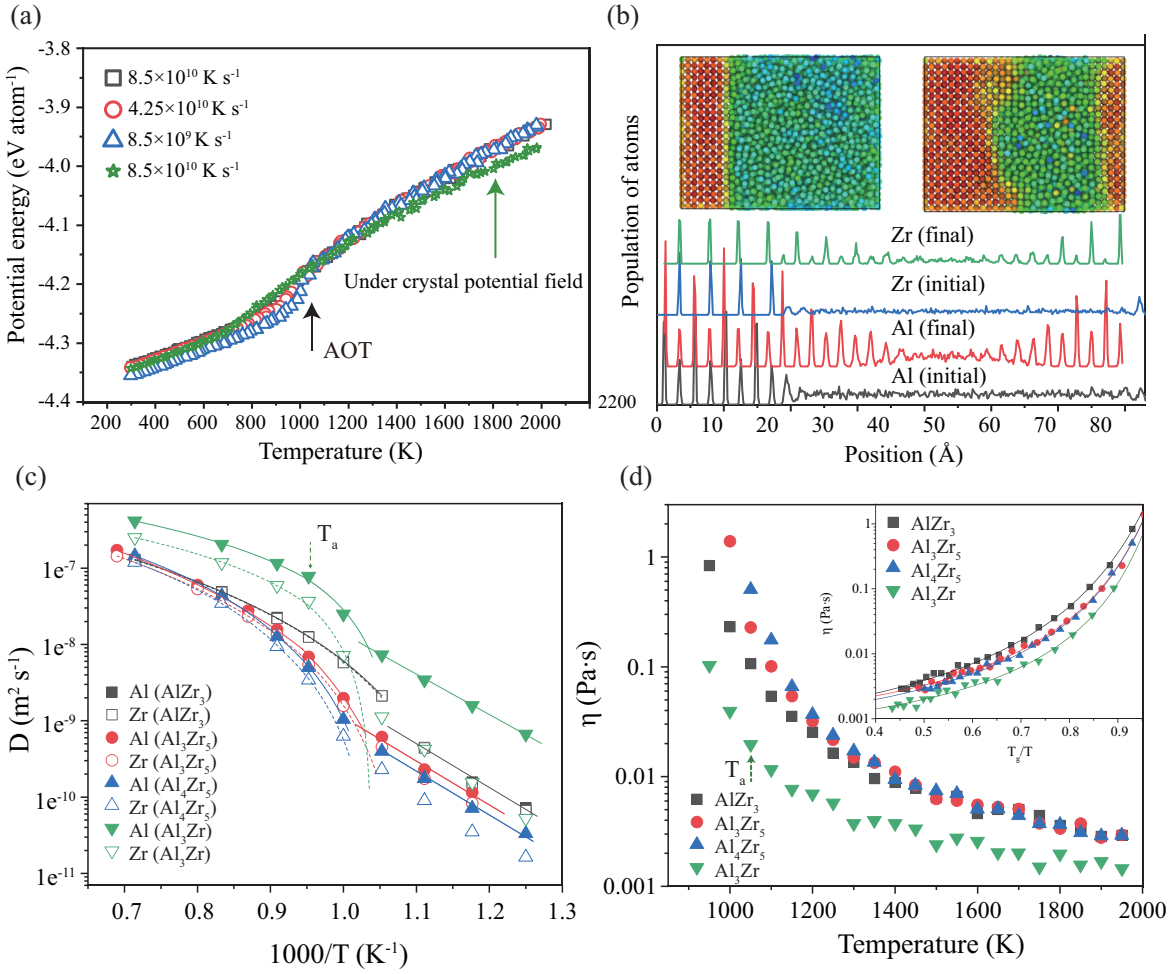

FIG. 1. (a) Potential energy per atom during continue rapid cooling for Al_3Zr. The cooling rates of 8.5×10^{10} K s^{-1}, 4.25×10^{10} K s^{-1}, and 8.5×10^{9} K s^{-1} were used in the simulations. (b) Atomic number density distribution under the condition of stable crystal potential field of Al_3Zr at a cooling rate of 8.5×10^{10} K s^{-1}. The snapshots are the solid-liquid model with close-packed plane constructed for Al_3Zr in the initial and final states, where the atoms are colored according to their respective BOO values. (c), (d) Temperature dependence of the self-diffusion coefficient D of Al and Zr (c) and viscosity η as well as the inset fitting plot (d) in the supercooled liquid state for $AlZr_3$, Al_3Zr_5, Al_4Zr_5, and Al_3Zr, respectively. T_a denotes the onset temperature of abnormal orderly transformation of Al_3Zr.

cooling rates was generally resulted from more adequate relaxation of the amorphous structure [69]. In contrast, the PE of Al_3Zr compound appears to remarkably decrease at around 1050 K, which is suspected to have the characteristics of orderly transformation. As the cooling rate decreases, this feature becomes more and more significant. Until this transition is proven to be related to conventional crystallization, we will temporarily call this behavior an AOT.

Figure 1(b) and Fig. S2 of the Supplemental Material [68] show the atomic number density distribution and snapshots of the solid-liquid model with close-packed plane constructed for each compound in the initial and final states, where the spheres represent the atoms colored according to their respective BOO values. Here, we examine the growth rate of crystals in a supercooled liquid with a continuous decrease in temperature in the presence of stable crystal potential field. By quenching at a rate of 8.5×10^{10} K s^{-1}, the crystal growth rates of the four compounds have shown distinguishability. From the visual characterization, it can be observed that the liquids of $AlZr_3$ and Al_4Zr_5 have been completely crystallized, supported by that the degree of structural order obtained is substantially the same as that of the stable crystalline phase. In sharp contrast, the Al_3Zr_5 liquid remains amorphous during the entire cooling process, and few signs of orderly arrangement of atoms were observed. The state of Al_3Zr is between $AlZr_3$ and Al_3Zr_5, that is, the supercooled liquid is only partially crystallized under the crystal potential field. The atomic number density distribution confirms that the final atomic distribution of $AlZr_3$ and Al_4Zr_5 have long-range order on the both sides of the original interface, but the compositional order in the final state is inconsistent to that of the stable crystal to some extent, which means that the supercooled liquid is transformed into metastable disordered crystal, rather than stable ordered crystal. Similar phenomenon can be observed in the crystalline part of Al_3Zr. This preferential precipitation of metastable disordered crystals under rapid cooling conditions can be easily explained kinetically, but only if there is a possibility in thermodynamics. In Fig. 1(a), we have inserted the change in the PE of Al_3Zr with temperature in the crystal potential field. Interestingly, the change in PE of the system,

compared with the case where there is no crystal potential field, becomes smoother with decreasing temperature, and no obvious abrupt change is observed. In the final state, the PE with a large number of crystalline structures is however higher than the PE after AOT without a crystalline potential field.

B. Kinetic properties upon rapid cooling

Figures S3(a)–S3(d) of the Supplemental Material [68] shows the log-log plot of mean squared displacement (MSD) versus time for each composition from the supercooled state to the glassy state. At high temperatures, the MSD of Al and Zr atoms increases linearly over a long period of time, and the slope enlarges with increasing temperature. When the temperature drops below 950 K, the linear relationship between time and MSD gradually disappears, indicating that the long-range diffusion of atoms is suppressed. Based on the MSD, self-diffusion coefficient D is calculated by using Einstein's relation at a long-time limit, $D = \lim_{t\to\infty} \frac{\langle(\Delta r)^2(t)\rangle}{6t}$, where $\langle(\Delta r)^2(t)\rangle$ represents the MSD. Figure 1(c) shows the temperature dependence of the self-diffusion coefficients of Al (D_{Al}) and Zr (D_{Zr}) in the supercooled liquid state for $AlZr_3$, Al_3Zr_5, Al_4Zr_5, and Al_3Zr, respectively. To facilitate visualization, the power law in mode-coupling theory [70] was introduced to fit the data above T_g, which clarifies the dynamics region where the Stokes-Einstein relationship [71,72] is violated. In the current system, this dynamic evolution is intensified with the increase of Al content, but it does not show a noticeable difference after the glass transition. We note that D_{Al} and D_{Zr} in the $AlZr_3$ supercooled liquid are extremely close, exhibiting strong cooperative motion of Al and Zr atoms. This observation is inconsistent with many studies, where smaller atoms were found to move more rapidly than the larger atoms in both metallic liquids and glasses [73]. As the Al concentration increases, D_{Al} and D_{Zr} start to deviate from each other by an increasing ratio of $D_{\mathrm{Al}}/D_{\mathrm{Zr}}$, which indicates the dynamic decoupling between Al and Zr atoms become more and more remarkable. In Al_3Zr, D_{Al} and D_{Zr} do not show significant kinetic inhibition when the AOT occurs, and rather, maintain much higher values compared to other compositions, which is particularly evident for Al species.

The fitting curves of viscosity are shown in the inset in Fig. 1(d), and the parameters are summarized in Table S1 of the Supplemental Material [68]. Generally, strong liquids with a smaller m exhibit smaller property changes during the glass transition since they have a stable structure with a high degree of short-range order [74]. However, fragile liquids with larger m display dramatic changes in properties in the glass transition range due to the lack of clear short-range order [75]. In the current system, the Al_3Zr supercooled liquid has the largest value of m. According to the physical meaning, the local structural stability of Al_3Zr supercooled liquid should be poor, which seems to echo the occurrence of AOT. From the temperature dependence of η as shown in Fig. 1(d), Al_3Zr supercooled liquid has significantly low η compared to other liquids at each corresponding temperature. This characteristic is consistent with the results of the temperature-dependent D.

The calculation results of the kinetic properties suggest that Al atoms in the Al-rich supercooled liquid have strong kinematic activity, and the impressive decoupling of D_{Al} and D_{Zr} indicates that the solute atoms have extremely limited inhibition of the movement of Al atoms. Whether the thermodynamic properties of supercooled liquid of the Al-rich alloy dominate this phenomenon is a question worthy of further study.

C. Thermodynamic signal of AOT

Figures 2(a) and 2(b) show the difference in enthalpy ΔH between the amorphous state and the stable crystalline or the metastable crystalline state for $AlZr_3$, Al_3Zr_5, Al_4Zr_5, and Al_3Zr, respectively. Glass transition temperature is derived from the viscosity fitting. By comparison, the ΔH between amorphous state and stable crystalline state for $AlZr_3$ and Al_3Zr is significantly larger than that for Al_3Zr_5 and Al_4Zr_5 in the supercooled liquid region. But this is obviously not necessarily related to the subsequent evolution of supercooled liquids. It is evident that glass transitions in $AlZr_3$, Al_3Zr_5, Al_4Zr_5 occur through a signal that ΔH decreases smoothly with decreasing temperature. In sharp contrast, a pronounced drop in ΔH is observed for Al_3Zr, of which the temperature is well above T_g. Therefore, some sort of orderly rather than glass transition occurs in Al_3Zr supercooled liquid. Note that the enthalpy of the transformation product, which can be treated as the formation enthalpy when the number of atoms for each species is equal, is markedly higher than that of the stable crystal ($\sim$5.5 kJ mol^{-1}) and the metastable crystal ($\sim$2.5 kJ mol^{-1}). From an energy point of view, the state of the AOT should be between the original amorphous and crystalline states.

Beyond the signal of phase transition provided by enthalpy, the Gibbs free energy, which introduces the effect of entropy, enable us to access the relative stability of competing phases at finite temperatures. Figure S4 of the Supplemental Material [68] plots the absolute vibrational entropy S^{vib} as a function of temperature. We found that at a temperature of $\sim$200 K above T_g, there is a discontinuous change in the relationship between S^{vib} and temperature of the supercooled liquid. In combination with mode-coupling theory, this sudden change in S^{vib} can correspond to a kinetic transition from diffusion to barrier hopping. Based on this clue, it appears that glass transition has also taken place in the Al_3Zr supercooled liquid after AOT, which is highly surprising. In addition, the S^{vib} of Al_3Zr liquid at high temperature is significantly higher than that after AOT, which indicates that the AOT is a process that greatly reduces the degree of disorder. Figures 2(c) and 2(d) show the difference in Gibbs free energy ΔG between the amorphous and crystalline states of $AlZr_3$, Al_3Zr_5, Al_4Zr_5, and Al_3Zr, respectively. As a whole, the change in ΔG of all alloys with temperature is similar to the shape of a spoon, with three different characteristic stages: ΔG linearly increases with the increasing degree of supercooling, ΔG decreases exponentially as it approaches T_g and ΔG remains essentially unchanged after glass transition. In the early stage of cooling, $AlZr_3$ and Al_4Zr_5 have considerably larger ΔG than Al_3Zr_5 and Al_3Zr with reference to stable or metastable crystals. This indicates that the thermodynamic driving force for phase transition of $AlZr_3$ and Al_4Zr_5 is much larger than that of Al_3Zr_5 and Al_3Zr. Obviously, the low S of Al_4Zr_5 supercooled liquid (see Fig. S4(c) of the Supplemental Material

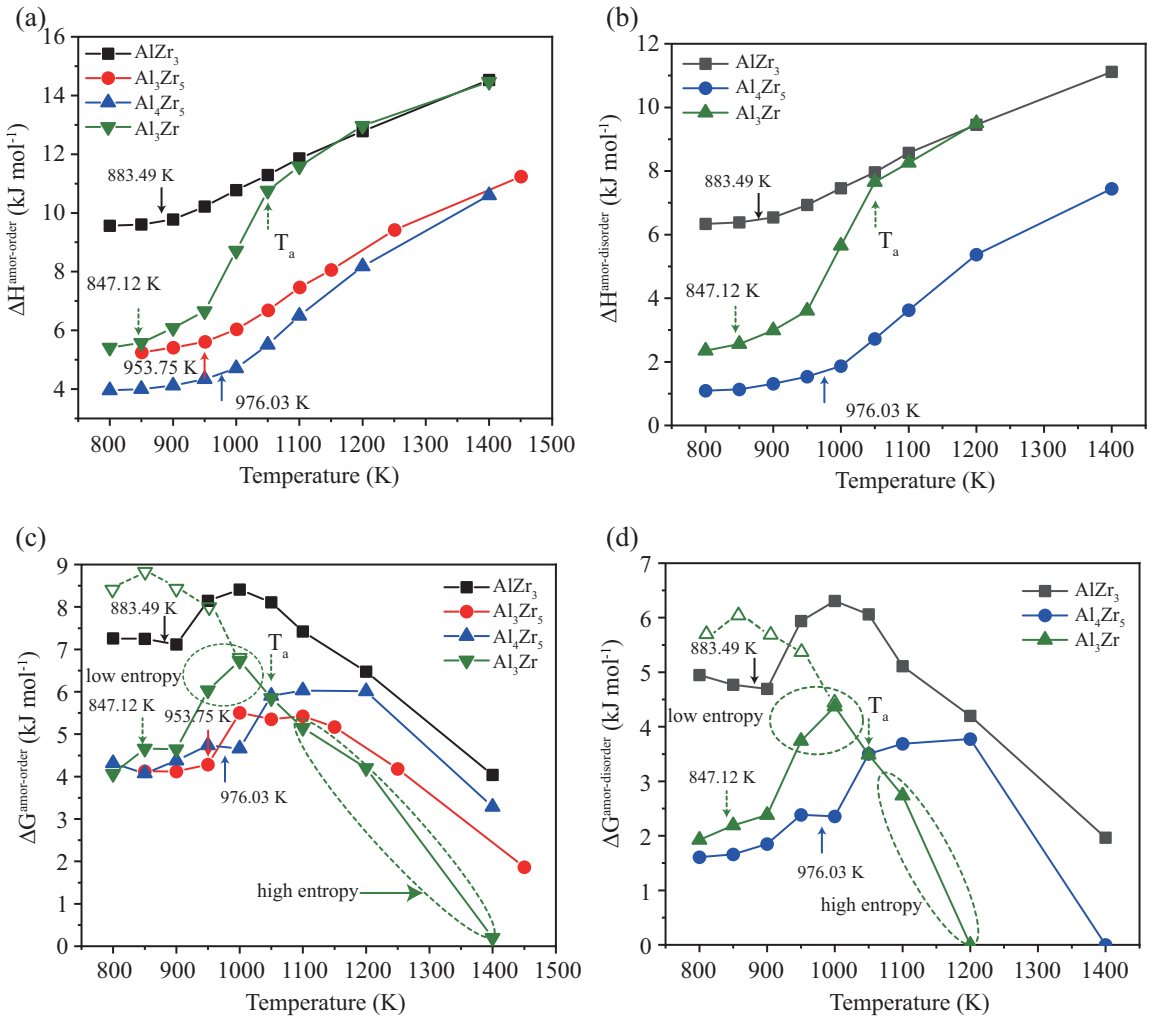

FIG. 2. (a) Difference in enthalpy $\Delta H^{\text{amor}-\text{order}}$ between amorphous and stable crystalline states. (b) Difference in enthalpy $\Delta H^{\text{amor}-\text{disorder}}$ between amorphous and metastable crystalline states. (c) Difference in Gibbs free energy $\Delta H^{\text{amor}-\text{order}}$ between amorphous and stable crystalline states. (d) Difference in Gibbs free energy $\Delta H^{\text{amor}-\text{disorder}}$ between amorphous and metastable crystalline states. The temperatures shown in the figure are T_g defined by the glass transition temperature of a viscosity equal to 10^{12} Pa · s, and T_a denotes the onset temperature of AOT in Al_3Zr supercooled liquid. The open symbols with dashed line represent a low-temperature epitaxy on the ΔG of the system without AOT.

[68]) reduces its stability relative to the corresponding crystal structure, although it has the lowest H [see Figs. 2(a) and 2(b)] at high temperature. Again, we detected the abnormality in the ΔG of Al_3Zr alloy. It can be seen that when the system is in a supercooled state, ΔG has predictable low value due to the contribution of high S, which results in a smaller driving force for the phase transition to the Al_3Zr compound. After AOT, compared with other alloys in the same state, the value of ΔG further increases by a larger amplitude. Although the formation enthalpy of the system is reduced during the AOT, the S of the orderly product is small relative to the crystal. Only after the end of the transition does the driving force for the phase transition return to a relatively low value. This result confirms that even if some orderly transformation occurs in the supercooled liquid of Al_3Zr, the product is essentially different from the stable or metastable crystal. In addition, we performed low-temperature epitaxy on the ΔG of the system based on the H and S of the high-temperature transition. It is found that if there is no AOT, the ΔG of the system will be much higher than the current value [dashed line in Figs. 2(c) and 2(d)], which proves that the AOT has played a positive role in reducing the free energy of the system.

D. Evolution of characteristic atomic structure during AOT

To clarify the structural correlation of thermodynamic and kinetic properties, we then compare the cluster packing efficiency (CPE), pair-distribution function (PDF), and CN of the supercooled liquid, glass, and crystalline states of these four compounds.

The CPE in this work is defined as the ratio of the atomic volume [76] based on RDF to the volume of the Voronoi mosaic cell (see details in Ref. [77]). Figure 3(a) and Fig. S5 of the Supplemental Material [68] illustrate the temperature dependence of CPE for $AlZr_3$, Al_3Zr_5, Al_4Zr_5, and Al_3Zr, respectively. For comparison, the average CPE of the amorphous structure, the stable crystalline structure, and the metastable crystalline structure are respectively shown in

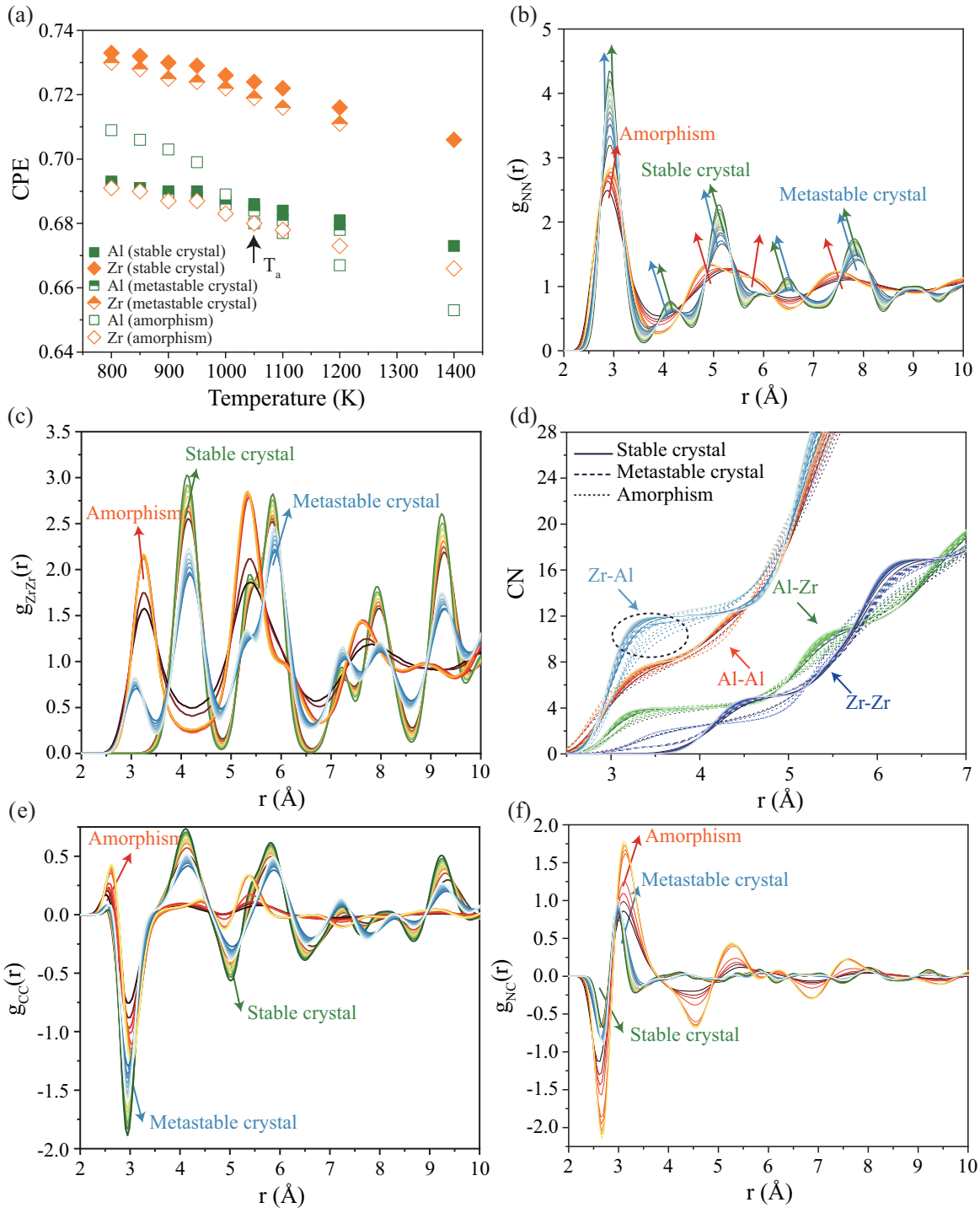

FIG. 3. (a) Temperature dependence of CPE of each species in the amorphous, stable crystalline, and metastable crystalline states of Al_3Zr. (b)–(f) $g_{NN}(r)$ (b), $g_{ZrZr}(r)$ (c), CN (*d*), $g_{CC}(r)$ (e), and $g_{NC}(r)$ (f) as a function of temperature for Al_3Zr in the amorphous (orange color system), stable crystalline (green color system), and the metastable crystalline (blue color system) states. The direction of the arrow in $g_{NN}(r)$ indicates the trend of the average atomic distance in each shell as the temperature decreases.

Figs. S5(a) and S5(b) of the Supplemental Material [68]. It is evident from $AlZr_3$, Al_3Zr_5, and Al_4Zr_5 that the CPE basically increases with the increasing Al content in the amorphous state. According to this rule, Al_3Zr should have a considerably high CPE in the supercooled liquid state. However, the actual situation has greatly deviated from expectations. We found that the CPE of Al_3Zr is far lower than expected value in the supercooled liquid state, and only sharply rise to a reasonable level after the occurrence of AOT. By analyzing the CPE of each species (see Figs. S5(c)–S5(e) of the Supplemental Material [68]), we know that for Al-depleted $AlZr_3$, Al_3Zr_5, and Al_4Zr_5, the CPE in the amorphous state is between stable or metastable crystalline states, and the CPEs of Al and Zr species are close in value. When the Al concentration is

increased to the alloy composition of Al_3Zr, the CPE of both species in the supercooled liquid is smaller than that of the stable or metastable crystal. After AOT, the CPE of Al species rather than Zr species increased sharply until it reached a normal value.

Figure 3(b) and Fig. S6 of the Supplemental Material [68] show the $g_{NN}(r)$ as a function of temperature for $AlZr_3$, Al_3Zr_5, Al_4Zr_5, and Al_3Zr, respectively. The peaks in $g_{NN}(r)$ correspond to interatomic distances in the range of 2 to 10 Å. It can be seen that when the four alloys are in the amorphous state, only the first and the third peaks move toward the increasing direction of r as the temperature decreases, and the remaining peaks move toward the direction to which r decreases. From this point of view, the change in gNN (r) of Al 3Zr with temperature conforms to the characteristics of the amorphous structure. Moreover, the amorphous nature of the Al_3Zr supercooled liquid become more prominent after AOT, that is, the splitting of the second peak is more notable. The position of the first peak continues to shift in the direction of increasing r. Figures S7–S9 of the Supplemental Material [68] provide $g_{AlAl}(r)$, $g_{AlZr}(r)$, and $g_{ZrZr}(r)$ for $AlZr_3$, Al_3Zr_5, Al_4Zr_5, and Al_3Zr as a function of temperature. We can see that the $g_{ij}(r)$ of these alloys in the supercooled liquid state show typical amorphous characteristics, including $g_{AlAl}(r)$ and $g_{AlZr}(r)$ of Al_3Zr. These characteristics is hardly affected by differences in crystal structure. After AOT, the amorphous characteristics of $g_{AlAl}(r)$ and $g_{AlZr}(r)$ of Al_3Zr appear to be more prominent, without any sign of transition to the crystal structure. However, it is also found that the amorphous features of $g_{ZrZr}(r)$ of Al_3Zr in the supercooled liquid are not obvious [see Fig. 3(c)]. Instead, after AOT, the second peak of the $g_{ZrZr}(r)$ shows slight split, which is even greater than other alloy compositions.

Further analysis was performed to obtain CN by $g_{ij}(r)$ integral, as shown in Fig. 3(d) and Fig. S10 of the Supplemental Material [68]. Obviously, the CN of the metastable crystalline structure is always closer to the amorphous structure than that of the stable crystalline structure. It is not difficult to understand that under rapid cooling condition, the supercooled liquid is more likely to meet the compositional requirements of the metastable structure, which is especially evident in the Al-Al atomic pair. Similar to $AlZr_3$ and Al_4Zr_5, in the amorphous state, the local composition of Al_3Zr is basically close to the corresponding crystalline state, and as a whole, there is no systematic deviation. An unusual point is that the CN of Zr-Al atomic pair changes significantly before and after AOT, and the average number of Al atoms around each Zr atom increases dramatically. Compared with other data, this should not be a single structural relaxation process caused by temperature decrease, but more like structural optimization.

The comparison of Bhatia-Thornton partial distribution function $g_{CC}(r)$ among stable ordered crystal, metastable disordered crystal, and amorphism for these four compounds are shown in Fig. 3(e) and Fig. S11 of the Supplemental Material [68]. In the amorphous state, the positions of the characteristic peaks of the four alloys in $g_{CC}(r)$ are basically identical but different in intensity. The peaks in $g_{CC}(r)$ reflect correlation between like chemical species as a function of distance, while troughs reflect cross correlation between unlike species. According to $g_{ij}(r)$, the small peak at ~2.5–2.6 Å relates to the Al-Al bonding interaction, while the sharp trough at around 3.0 Å reflects the strong correlation of Al-Zr pair. In the medium range, small troughs at ~5.0 Å and ~6.0 Å are featured by unlike species, and the peak between them represents Zr species. From Fig. 3(e) and Fig. S11 of the Supplemental Material [68], the local composition of supercooled liquids and their respective crystals has a strong correlation within the nearest atomic neighbors, but this correlation becomes less significant beyond the next-nearest atomic neighbors. There is no essential difference between Al-rich and Al-depleted alloys. We noticed that, compared with other compositions, the order of local composition in Al_3Zr supercooled liquid increases rapidly with decreasing temperature. Especially after AOT, this local compositional ordering has been greatly strengthened in the medium range. However, the peak position is still far from the characteristic peak of the corresponding crystalline structure, and thus, it is more like an enhanced amorphous structure.

Figure 3(f) and Fig. S12 of the Supplemental Material [68] show the comparison of $g_{NC}(r)$ for these compounds in various states. It is interesting to note that the profile of $g_{NC}(r)$ for Al-depleted compounds show little difference in the amorphous state, although $AlZr_3$ and Al_4Zr_5 differ greatly in the ratio of Al and Zr species. The positive peaks at ~2.7–2.8 Å in $g_{NC}(r)$ of $AlZr_3$, Al_3Zr_5, and Al_4Zr_5 indicate that the atomic density around Al atoms is higher than that around Zr atoms at this distance. A negative peak at ~3.4 Å means that there are more atoms around Zr atoms than Al atoms. Similarly, the next positive and negative peaks repeat this manner at ~4.75 Å and ~5.5 Å, respectively. In sharp contrast, the $g_{NC}(r)$ of the Al-rich compounds Al_3Zr exhibits completely opposite profiles, indicating a fundamental change in the way of atomic close-packing. If we simply treat a small number of atoms as solute, the atomic packing manner of this binary system basically conforms to the solute-centered cluster structure model [28,78]. From the calculation results of $g_{NC}(r)$, we also observe the nonlinear dependence of atomic close-packing on temperature in the supercooled liquid of Al-rich Al_3Zr. After AOT, the original atomic close-packing manner has not changed, but has been greatly strengthened. In other words, while the supercooled liquid remains amorphous, the number of atoms around the Al and Zr atoms increases significantly.

IV. DISUSSIONS

A. Enhanced compositional heterogeneity by AOT

Evidences from thermodynamic property, kinetics property, and atomic structure have strongly suggested that under the condition of rapid cooling, the Al-rich alloy Al_3Zr definitely undergo AOT, which further distances the supercooled liquid from its crystalline counterpart and evolves into a more typical amorphous state. Before clarifying the physical nature of this phenomenon and its impact on subsequent phase transition paths, we first outline the main characteristics of AOT based on available information: (1) with the corresponding crystalline phase as the reference state, the mixed H of the supercooled liquid is greatly reduced. Although S^{vib} and S^{conf} become smaller, the Gibbs free energy of

supercooled liquid still decreases as a whole; (2) the diffusion coefficient D before and after AOT still follow the power law, and the dynamic characteristics have not fundamentally changed, that is, the system is still in a supercooled liquid state instead of a solid state; (3) in the short and medium range, the order of the composition and structure as well as the atomic packing density have been greatly improved. This ordered and densified product is not related to the corresponding stable or metastable crystal, and instead, retains the characteristics of the amorphous structure.

The simulation results of grain growth and continuous cooling highlight the contradiction between the stable or metastable crystal and the product of AOT. Under the corresponding stable crystal potential field, the crystallization rate of Al_3Zr supercooled liquid is not fast compared with $AlZr_3$ and Al_4Zr_5. In the absence of a crystal potential field, the Al_3Zr supercooled liquid can readily undergo an orderly transformation. By combining the results of Figs. 1(a) and 2(a), if a stable crystal potential field exists, then the AOT in the Al_3Zr supercooled liquid is suppressed, which is supported by the fact that the atomic potential energy of the crystalline/amorphous state is higher than that of the completely amorphous state at the same cooling rate. These phenomena seem to deviate severely from the classical theory.

To prove this deviation, we use the data obtained in this work to theoretically evaluate the crystal growth rate within the framework of classical nucleation theory (CNT). The results are shown in Fig. S13 of the Supplemental Material [68], including the cases of stable ordered and metastable disordered crystals. Intriguingly, for Al-depleted compounds, i.e., $AlZr_3$, Al_3Zr_5, and Al_4Zr_5, the theoretical grain growth rate is fully consistent with the results observed in practice (see Fig. 1(b) and Fig. S2 of the Supplemental Material [68]). For the Al-rich compound Al_3Zr, the predicted value greatly overestimates the observed grain growth rate. Considering that the grain growth rate is a physical quantity related to the properties of both the crystal and the liquid, when the structure and properties of the crystal are specific, the origin of this large deviation can only come from liquid. That is, the structure and properties of the supercooled liquid obtained under rapid cooling conditions may have deviated severely from those of the homogeneous solution having the same composition.

To gain a deeper understanding of this phenomenon, we can start with the composition and structure of the local atomic clusters. On the one hand, if large-scale compositional heterogeneity occurs in the system, then the composition of each microdomain deviates from that of the original compound. In this case, the crystal potential field cannot effectively guide the orderly arrangement of nearby atoms in the supercooled liquid, but time-consuming composition fluctuations must be performed first, which will cause the growth rate of the compound grains to decrease. On the other hand, if the local atomic clusters characterized by spatial topology after AOT are fundamentally different from the corresponding crystalline structure, then the crystal potential field and AOT will also tend to form competition, thereby hindering the growth of the corresponding stable or metastable crystals. To verify these hypotheses, we introduced the concept of Al medium-range cluster (MRC), which depicts the size and number of

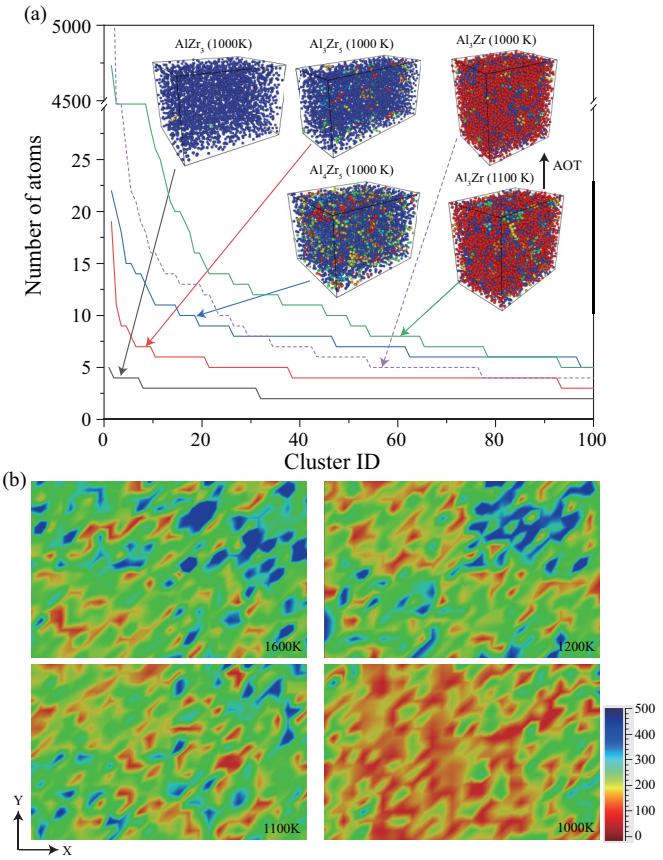

FIG. 4. (a) Distribution of the number and size of Al clusters for these alloys in the supercooled liquid state. The data of Al_3Zr at 1100 K and 1000 K are given to examine the changes before and after AOT. MRCs are identified by the rainbow color system according to the size from the largest MRC to the smallest MRC in ascending order, in which blue presents the smallest one and red the largest one. (b) Projections of Al MRC on the x-y plane at 1600 K, 1200 K, 1100 K, and 1000 K, respectively, for Al_3Zr. The value at each coordinate equals to the average cluster identification number corresponding from the largest MRC to the smallest MRC in ascending order along the z direction. Al atoms are colored according to the MRC to which they belong.

Al atoms that form a network structure in real space. Based on the average interatomic distance of Al, the cutoff radius was set to 2.7 Å. Figure 4(a) shows the distribution of the number and size of Al clusters in real space for these alloys in the supercooled liquid state. For Al_3Zr, the data at 1100 and 1000 K are presented to check the changes before and after AOT. From Fig. 4(a), the size of each Al MRC in the supercooled liquid of Al-depleted alloys is on the same order of magnitude, and the number of Al atoms contained in the largest MRC is comparable. For Al-rich Al_3Zr, the number of atoms in the largest Al MRC increases sharply to 4733. After AOT, this number even increases to 5942, and what remain are a large number of tiny Al clusters separated from each other. Obviously, AOT changes the distribution of Al atoms in the supercooled liquid and enhances the heterogeneity of the composition. To facilitate the observation of the evolution of Al MRC in the supercooled liquid, we plotted the projections of Al MRC on the x-y plane at 1600 K, 1200 K, 1100 K, and

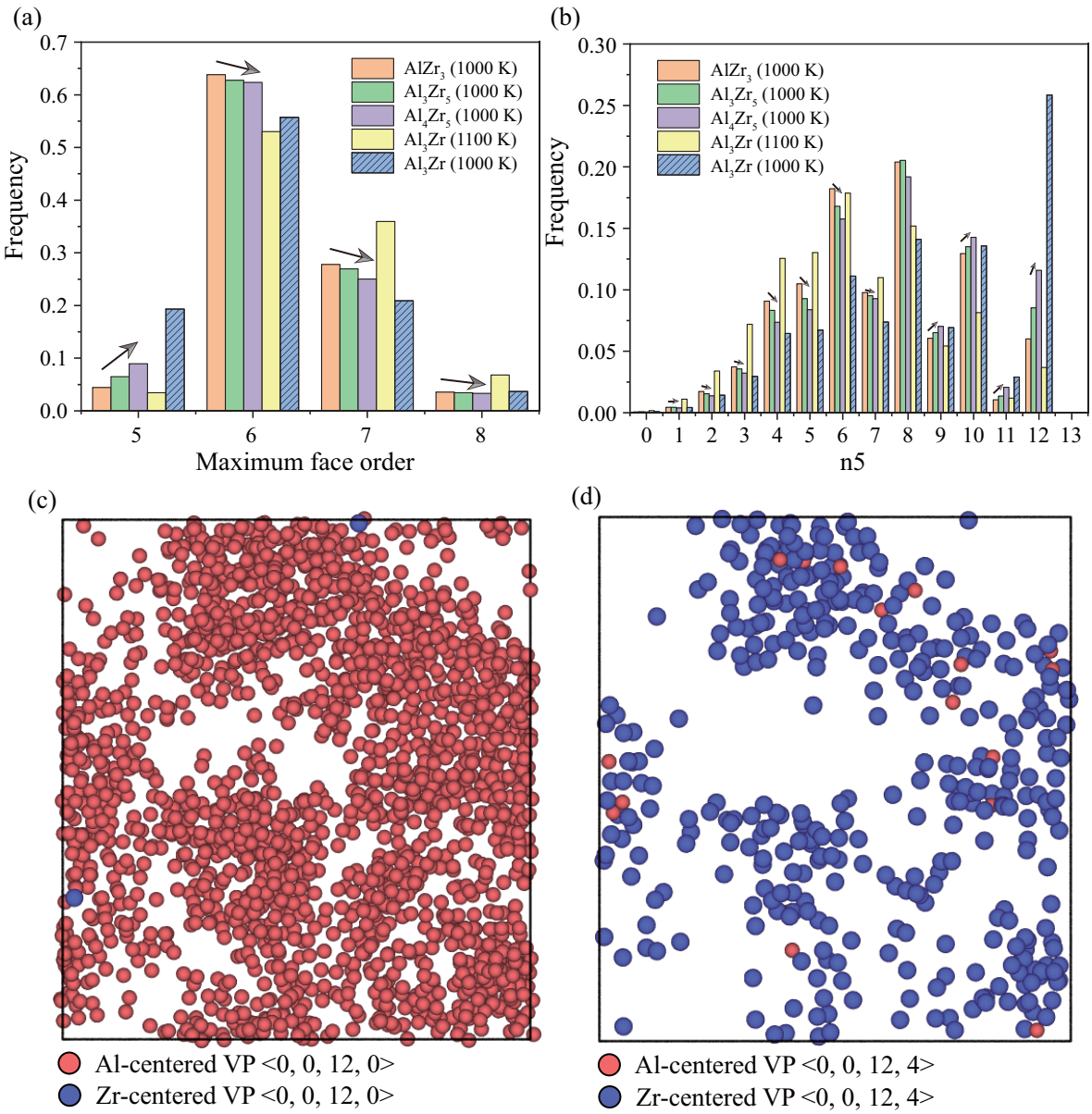

FIG. 5. (a), (b) Number of maximum face order (maximum value of i for non-zero n in n_i) (a) and number of pentagonal faces (n_5) (b) of $AlZr_3$, Al_3Zr_5, Al_4Zr_5, and Al_3Zr, respectively, in the supercooled liquid state. The data after AOT for Al_3Zr is shaded. The arrow indicates the changing trend of each data when the Al content is less than 75%. (c), (d) Al-centered or Zr-centered VP $\langle 0, 0, 12, 0\rangle$ (c) and Al-centered or Zr-centered VP $\langle 0, 0, 12, 4\rangle$ (d) in Al_3Zr after AOT.

1000 K, respectively, as seen in Fig. 4(b). The results prove that the heterogeneity of the components is common in Al-rich supercooled liquid, and the AOT further enhances this heterogeneity, which is consistent with the statistical results in $g_{CC}(r)$ [see Fig. 3(e)]. Since it is uncertain whether the liquid structure before and after AOT remains the same, strictly speaking, this phenomenon may not be defined as the phase separation mentioned in the experimental works [44,46,79–81]. In any case, the heterogeneity of the components in the Al_3Zr supercooled liquid enhanced by AOT is the reason why the grain growth rate of the stable compound is much lower than the theoretical prediction.

B. Origin of AOT in the Al-rich side upon rapid cooling

To define the AOT in essence, in addition to the composition, changes in the atomic structure must be quantified. In this work, Voronoi polyhedral (VP) index [77] denoted by $\langle n_3, n_4, n_5, n_6, \ldots, n_i, \ldots\rangle$, where n_i represents the number of i-edge polygons, was introduced to analyze the change in the amorphous atomic structure. In the present work, the quartet notation $\langle n_3, n_4, n_5, n_6\rangle$ is used to describe the atomic structure. Figures 5(a) and 5(b) show the feature of atomic structure of $AlZr_3$, Al_3Zr_5, Al_4Zr_5, and Al_3Zr in the supercooled liquid state, by taking the number of maximum face order (maximum value of i for nonzero n in n_i) and the number

of pentagonal faces (n_5) as indicators. It is clear from the histogram that when the Al-depleted alloy is in the supercooled liquid state, the characteristics of the amorphous atomic structure and the Al content have a monotonic correlation. When the Al content is increased until the alloy is in an Al-rich state, this monotonicity is completely destroyed. It can be seen that before AOT, the number of pentagons of atomic structure in the supercooled liquid is reduced, while the proportions of heptagons and octagons increase largely. Combined with the information provided by this work, these heptagons and octagons appearing in large numbers in supercooled liquid have caused two serious consequences. One is excessively high ΔH [see Figs. 2(a) and 2(b)], and the other is extremely low CPE [see Fig. 3(a)]. To our surprise, after AOT, these unfavorable situations have undergone fundamental changes. It can be seen that the proportions of various polygons have undergone major adjustments. A large number of heptagon and octagon have disappeared and replaced by pentagons and a small number of hexagons. Based on the composition dependence of the number of polygons, AOT seems to be bringing the system back to a reasonable state. Figure 5(b) specifically shows the number of pentagons in each VP. An energetically stable VP in the supercooled liquid generally has more than 10 pentagons, e.g., $\langle 0, 0, 12, 0\rangle$, $\langle 0, 1, 10, 2\rangle$, $\langle 0, 0, 12, 2\rangle$, $\langle 0, 0, 12, 3\rangle$, and $\langle 0, 0, 12, 4\rangle$, depending on the size ratio of the atoms [82,83]. Obviously, in the supercooled liquid of Al_3Zr before AOT, a large number of Voronoi polyhedrons with pentagon numbers less than 9 initially exists. As mentioned earlier, this violates the monotonic correlation between the number of pentagons and the composition of alloy. After AOT, the number of VPs with more than 9 pentagons increased dramatically, and stable icosahedral clusters characterized by 12 pentagons finally dominate the atomic structure of the supercooled liquid. This plays a key role in improving the stability of the supercooled liquid, which is mainly reflected in the greatly reduced ΔH [see Figs. 2(a) and 2(b)] and the improved CPE (see Fig. 3(a) and Figs. S5(a) and S5(b) of the Supplemental Material [68]). A slightly decrease in S does not prevent the reduction of the ΔG [see Figs. 2(c) and 2(d)].

The correlation between local composition and structure is an important physical origin that determines the properties and heterogeneity of supercooled liquids. By considering the CN of the species [see Fig. 3(d)], we specified VPs $\langle 0, 0, 12, 0\rangle$ (Icosahedral cluster or ICO for short) and $\langle 0, 0, 12, 4\rangle$, the two most stable and highest proportions of the characteristic polyhedrons to characterize the microstructure of an Al-rich supercooled liquid. The results are shown in Figs. 5(c) and 5(d). Interestingly, all stable ICOs are centered on Al atoms and exhibit significant enrichment. And almost all stable VP $\langle 0, 0, 12, 4\rangle$ are centered on Zr atoms and attached to the enriched region of the ICO. To be sure, these rich ICO and VP $\langle 0, 0, 12, 4\rangle$ solvent-solute regions play a positive role in reducing G and increasing CPE of the system. This special local atomic structure with obvious compositional differences was not found in Al-depleted alloys, including $AlZr_3$ which has the same atomic ratio as Al_3Zr (see Figs. S14(a), S14(c), and S14(e) of the Supplemental Material [68]).

At this point, we first give a general overview of the process and causes of AOT in Al-rich supercooled liquid. When the supercooled liquid is at a higher temperature, the S term in G that determines the stability of system dominates. Increasing the disorder of the atomic vibration and arrangement is beneficial to maintaining the stability of the liquid. However, blindly increasing the disorder cause a large number of thermally unfavorable local atomic clusters in the supercooled liquid, which are specifically manifested as low CPE and high ΔH. This is determined by the inherent properties of alloying elements. When the temperature drops rapidly, the positive effect of the S term in G decreases sharply, while the negative effect of the H term becomes crucial. To further reduce G to improve stability, the supercooled liquid in an unstable state will first adjust itself to a more stable state rather than crystallize into a stable compound, which follows Ostwald's step rule. Unfortunately, in the current state where Al and Zr atoms are completely randomly mixed, it is impossible to reduce ΔH or improve CPE by directly rearranging local atoms. To this end, the supercooled liquid preferentially adjusts the local composition, thereby forming nanoscale reformed Al-rich and Al-depleted regions. This adjustment enables local atomic clusters to undergo stabilizing transitions and improve cluster packing efficiency, thereby reducing G of the entire system. In this case, the considerable diffusion coefficient and dynamic decoupling in Al-rich supercooled liquid [see Fig. 1(c)] do not play a positive role in the nucleation and growth of the crystal grains of stable compound, but greatly promotes the stabilization process of supercooled liquid.

AOT is a thermodynamic behavior of an Al-rich supercooled liquid to maintain its stability under rapid cooling conditions. Whether the supercooled liquid after AOT contributes to subsequent glass transition depends mainly on the type and distribution of the local atomic clusters generated. Previous studies have shown that crystal nucleation begins with the formation of MRC, rather than short-range cluster (SRC) with structures similar to subsequent nucleated crystals [84,85]. Local aggregation of ICO and ICO-like (VPs $\langle 0, 2, 8, 2\rangle$ and $\langle 0, 1, 10, 2\rangle$) clusters in supercooled liquid can effectively promote the formation of new nuclei [86]. Experimental results further confirm that FCC crystals can be formed in supercooled liquids by heteroepitaxial growth from an ICO quasicrystals template [87,88]. This process will be completed at a very fast rate particularly in a single-component or near-one-component system, showing extremely poor GFA [89]. The reformed Al-rich region resulted from AOT has a feature similar to a single-component system. If there are a large number of ICO/ICO-like MRCs in the Al-rich region, these MRCs can well serve as precursors of the FCC-Al nuclei, which are readily transformed to FCC-Al during cooling, or precipitated FCC-Al nanocrystals by heating treatment in a nondiffusive manner.

Figure 6(a) depicts the evolution of Al-centered ICO MRCs of the Al_3Zr supercooled liquid quenched to 1000 K. We assume that ICO MRCs with central atoms less than 50 are difficult to serve as precursors of the FCC-Al nuclei. They are considered as isolated clusters and shown in blue. Otherwise, ICO MRCs of different sizes are marked by rainbow color scheme. Note that only the central atoms of each ICO but ICO-like (∼20% in each MRCs) are presented in Fig. 6(a), and thus the actual size of the ICO/ICO-like MRCs

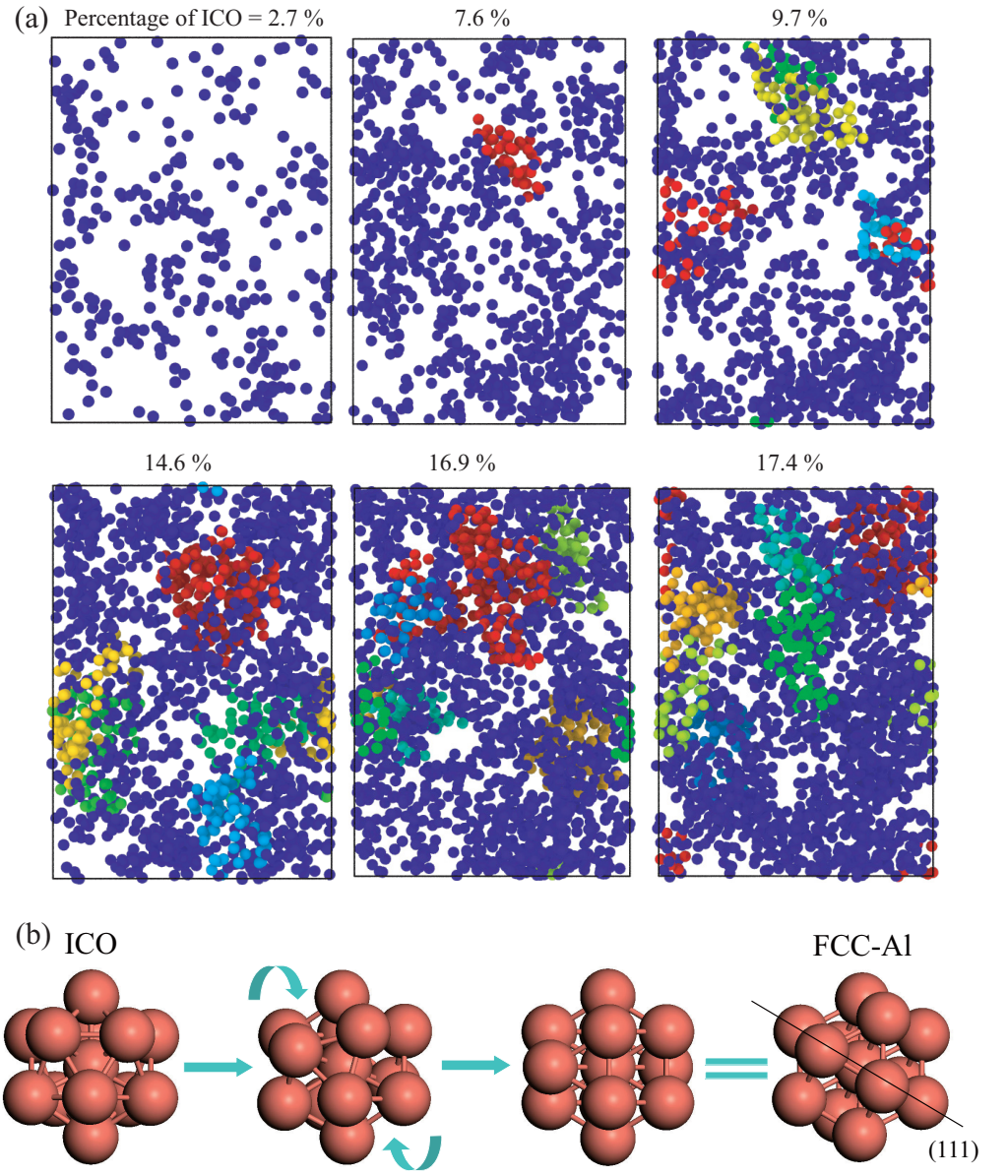

FIG. 6. (a) Distribution of Al-centered ICO MRCs as simulation time increases in the supercooled liquid of Al_3Zr rapidly quenched to 1000 K, where the AOT occurs. The different ICO MRCs with central atoms more than 50 are marked by rainbow color scheme except for blue, which represents the isolated clusters. (b) Scheme of transformation from each ICO unit in the ICO MRC to FCC-Al cluster or nucleation in a possible easy way.

should be larger than the size shown. Obviously, with the progress of AOT, the number and size of ICO MRCs that potentially server as precursors of FCC-Al nuclei constantly increase and dispersed in supercooled liquid. Moreover, the stable Zr-centered VPs ⟨0, 0, 12, 4⟩ are distributed mainly on the edge of Al-centered ICO and ICO-like MRCs, which can effectively prevent the rapid growth of FCC-Al nanocrystals [90,91]. These are essentially in line with our hypothesis that the consequence of AOT is to make the supercooled form a microstructure, which is quite favorable for the precipitation of dispersed FCC-Al nanocrystal nuclei in the amorphous matrix [a scheme of transformation from each ICO unit in the ICO MRC to FCC-Al cluster or nucleation in a possible easy way is shown in Fig. 6(b)]. This phenomenon can be hardly observed in the supercooled liquid of Al-depleted alloys (see Figs. S14(b), S14(d), and S14(f) of the Supplemental Material [68]).

All these observations and findings are enough to give us some insights. If the supercooled liquid obtained by rapid cooling is regarded as a solid solution matrix and unstable low-density clusters are considered as point defects containing voids, the process of the solvent or solute atoms diffusing into the defective regions and precipitating the stabilized MRCs is exactly equivalent to the formation of the Guinier-Preston zone in Al-based alloy. Therefore, the AOT in supercooled liquid that includes two basic stages of directional diffusion and stabilization of defect clusters can be well compared to the aging process of Al-based solid solution after quenching. We believe that the AOT of Al-based alloy melts in the supercooled state make the complete amorphization ability of

Al-based melts significantly poorer than that of other alloy systems such as Fe-based alloys, which can effectively control the local ordered structure in the supercooled liquid through alloying [92].

In view of the characteristics of AOT, the preparation of Al-based BMG by the conventional melt quenching method seems mechanically unfeasible, that is, it is difficult to simultaneously meet the requirements of both the cooling rate and the stability of the amorphous structure. In addition, the AOT causes the microstructure and properties of the supercooled liquid to deviate greatly from the initial state, which means that the traditional BMG composition design methods to determine the composition range of Al-based BMG are likely to fail. From the mechanism of AOT, the close-packing principle can more effectively evaluate the GFA of Al-based alloys, thereby guiding the composition design of high-strength FCC-Al/amorphous dual-phase nanomaterials.

V. CONCLUSIONS

We use molecular dynamics simulation technique to study the evolution of atomic structure of Al-Zr alloy in supercooled liquid state under rapid cooling conditions. Through the quantitative characterization of the thermodynamic properties, kinetic properties and atomic structure of Al-Zr alloys with different compositions from the Al-depleted side to the Al-rich side, we found that the Al-rich supercooled liquid, i.e., Al_3Zr in this work, has a much lower cluster packing efficiency and high Gibbs free energy than Al-depleted ones, causing the Al_3Zr supercooled liquid to be in an unstable state. To keep the system in a thermodynamically stable state, an abnormal orderly transformation featured by two stages of directional diffusion and stabilization of defect clusters takes place in the Al_3Zr supercooled liquid. In this way, the cluster packing efficiency in nanoscale reformed Al-rich region substantially increases, by which the Gibbs free energy of the entire system is reduced to a relatively low level. However, the reformed Al-rich region by abnormal orderly transformation is structurally helpful in promoting the precipitation of dispersed FCC-Al nanocrystal nuclei in the amorphous matrix, which contributed to the poor complete amorphization ability of Al-based melts compared to other systems.

ACKNOWLEDGMENT

This work was supported by the National Natural Science Foundation of China (Grants No. 51831007 and No. 51601160), National Key R&D program of China (Grant No. 2017YFB0702901).

[1] A. Inoue, Bulk glassy alloys: Historical development and current research, Engineering **1**, 185 (2015).
[2] J. Schroers, Processing of bulk metallic glass, Adv. Mater. **22**, 1566 (2010).
[3] A. Inoue, K. Ohtera, K. Kita, and T. Masumoto, New amorphous alloys with good ductility in Al-Ce-M (M = Nb, Fe, Co, Ni or Cu) systems, Jpn. J. Appl. Phys. **27**, L1796 (1988).
[4] H. A. Davies and J. B. Hull, An amorphous phase in a splat-quenched A1-17.3 at %Cu alloy, Scr. Metall. **6**, 241 (1972).
[5] Z. P. Chen, J. E. Gao, Y. Wu, H. X. Li, H. Wang, and Z. P. Lu, Role of rare-earth elements in glass formation of Al–Ca–Ni amorphous alloys, J. Alloys Compd. **513**, 387 (2012).
[6] H. Yang, J. Q. Wang, and Y. Li, Influence of TM and RE elements on glass formation of the ternary Al–TM–RE systems, J. Non Cryst. Solids **354**, 3473 (2008).
[7] Y. He, G. J. Shiflet, and S. J. Poon, Synthesis and properties of aluminum-based metallic glasses containing rare earths, J. Alloys Compd. **207-208**, 349 (1994).
[8] F. Guo, S. Enouf, G. Shiflet, and J. Poon, Role of atomic size on glass formability and thermal stability of Al-based amorphous alloys, Mater. Trans., JIM **41**, 1406 (2000).
[9] J. F. Löffler, Recent progress in the area of bulk metallic glasses, Z. Metallk. **97**, 225 (2006).
[10] J. Henao, A. Concustell, I. G.Cano, S. Dosta, N. Cinca, J. M. Guilemany, and T. Suhonen, Novel Al-based metallic glass coatings by Cold Gas Spray, Mater. Des. **94**, 253 (2016).
[11] B. J. Yang, J. H. Yao, J. Zhang, H. W. Yang, J. Q. Wang, and E. Ma, Al-rich bulk metallic glasses with plasticity and ultrahigh specific strength, Scripta Mater. **61**, 423 (2009).
[12] A. Inoue and H. Kimura, Fabrications and mechanical properties of bulk amorphous, nanocrystalline, nanoquasicrystalline alloys in aluminum-based system, J. Light Met. **1**, 31 (2001).
[13] Y. He, G. M. Dougherty, G. J. Shiflet, and S. J. Poon, Unique metallic glass formability and ultra-high tensile strength in Al-Ni-Fe-Gd alloys, Acta Metall. Mater. **41**, 337 (1993).
[14] J. M. Freitag, R. G. Koknaev, R. Sabet-Sharghi, M. Koknaeva, and Z. Altounian, Mechanical properties of Al–Y–Ni amorphous ribbons, J. Appl. Phys. **79**, 3967 (1996).
[15] J. Mu, H. Fu, Z. Zhu, A. Wang, H. Li, Z. Hu, and H. Zhang, Synthesis and Properties of Al-Ni-La Bulk Metallic Glass, Adv. Eng. Mater. **11**, 530 (2009).
[16] A. Inoue, Amorphous, nanoquasicrystalline and nanocrystalline alloys in Al-based systems, Prog. Mater Sci. **43**, 365 (1998).
[17] H. W. Sheng, Y. Q. Cheng, P. L. Lee, S. D. Shastri, and E. Ma, Atomic packing in multicomponent aluminum-based metallic glasses, Acta Mater. **56**, 6264 (2008).
[18] Z. Zhang, X. Z. Xiong, W. Zhou, X. Lin, A. Inoue, and J. F. Li, Glass forming ability and crystallization behavior of Al–Ni–RE metallic glasses, Intermetallics **42**, 23 (2013).
[19] R. S. Maurya and T. Laha, Effect of rare earth and transition metal elements on the glass forming ability of mechanical alloyed Al–TM–RE based amorphous alloys, J. Mater. Sci. Technol. **31**, 1118 (2015).
[20] Y. He, S. J. Poon, and G. J. Shiflet, Synthesis and properties of metallic glasses that contain aluminum, Science **241**, 1640 (1988).
[21] B. A. Sun, M. X. Pan, D. Q. Zhao, W. H. Wang, X. K. Xi, M. T. Sandor, and Y. Wu, Aluminum-rich bulk metallic glasses, Scripta Mater. **59**, 1159 (2008).
[22] F. Czerwinski, Cerium in aluminum alloys, J. Mater. Sci. **55**, 24 (2020).

[23] X. M. Shi *et al.*, Structure alterations in Al-Y-based metallic glasses with La and Ni addition, J. Appl. Phys. **119**, 114904 (2016).
[24] M. Yan, J. Q. Wang, G. B. Schaffer, and M. Qian, Solidification of nitrogen-atomized $Al_{86}Ni_6Y_{4.5}Co_2La_{1.5}$ metallic glass, J. Mater. Res. **26**, 944 (2011).
[25] W. J. Botta, C. T. Rios, R. D. Sá Lisboa, A. R. de Andrade, M. F. de Oliveira, C. Bolfarini, and C. S. Kiminami, Crystallisation behaviours of Al-based metallic glasses: Compositional and topological aspects, J. Alloys Compd. **483**, 89 (2009).
[26] L. Zhuo and T. Zhang, Studies on the formability of Al-based metallic glasses/nanocomposites based on isochronal DSC analysis, J. Non Cryst. Solids **356**, 2258 (2010).
[27] R. I. Wu, G. Wilde, and J. H. Perepezko, Glass formation and primary nanocrystallization in Al-base metallic glasses, Mater. Sci. Eng., A **301**, 12 (2001).
[28] D. B. Miracle, A structural model for metallic glasses, Nat. Mater. **3**, 697 (2004).
[29] J. C. M. Pirajáan, *Thermodynamics: Kinetics of Dynamic Systems* (IntechOpen, London, 2011).
[30] Z. P. Lu and C. T. Liu, A new glass-forming ability criterion for bulk metallic glasses, Acta Mater. **50**, 3501 (2002).
[31] N. A. Mauro, M. Blodgett, M. L. Johnson, A. J. Vogt, and K. F. Kelton, A structural signature of liquid fragility, Nat. Commun. **5**, 4616 (2014).
[32] Y. Q. Cheng and E. Ma, Atomic-level structure and structure–property relationship in metallic glasses, Prog. Mater Sci. **56**, 379 (2011).
[33] K. K. C. Chan and J. S. Viñas, *Metallic Glasses* (MDPI AG, Basel, 2018).
[34] A. L. Greer, Confusion by design, Nature **366**, 303 (1993).
[35] A. Inoue, Stabilization of metallic supercooled liquid and bulk amorphous alloys, Acta Mater. **48**, 279 (2000).
[36] Z. P. Lu and C. T. Liu, Glass Formation Criterion for Various Glass-Forming Systems, Phys. Rev. Lett. **91**, 115505 (2003).
[37] J. H. Perepezko, J. Hamann, R. J. Hebert, H. Rösner, and G. Wilde, Amorphization and devitrification reactions in metallic glass alloys, Mater. Sci. Eng., A **449-451**, 84 (2007).
[38] W. G. Stratton, J. Hamann, J. H. Perepezko, P. M. Voyles, X. Mao, and S. V. Khare, Aluminum nanoscale order in amorphous $Al_{92}Sm_8$ measured by fluctuation electron microscopy, Appl. Phys. Lett. **86**, 141910 (2005).
[39] D. R. Allen, J. C. Foley, and J. H. Perepezko, Nanocrystal development during primary crystallization of amorphous alloys, Acta Mater. **46**, 431 (1998).
[40] Z.-H. Zhong and L. Nilsson, A unified contact algorithm based on the territory concept, Comput. Method Appl. M. **130**, 1 (1996).
[41] Y. E. Kalay, L. S. Chumbley, and I. E. Anderson, Crystallization behavior in a highly driven marginal glass forming alloy, J. Non Cryst. Solids **354**, 3040 (2008).
[42] D. V. Louzguine and A. Inoue, Investigation of structure and properties of the Al–Y–Ni–Co–Cu metallic glasses, J. Mater. Res. **17**, 1014 (2002).
[43] J. H. Perepezko, R. J. Hebert, and W. S. Tong, Amorphization and nanostructure synthesis in Al alloys, Intermetallics **10**, 1079 (2002).
[44] J. Antonowicz, M. Kędzierski, E. Jezierska, J. Latuch, A. R. Yavari, L. Greer, P. Panine, and M. Sztucki, Small-angle X-ray scattering from phase-separating amorphous metallic alloys undergoing nanocrystallization, J. Alloys Compd. **483**, 116 (2009).
[45] D. H. Kim, W. T. Kim, E. S. Park, N. Mattern, and J. Eckert, Phase separation in metallic glasses, Prog. Mater Sci. **58**, 1103 (2013).
[46] A. K. Gangopadhyay, T. K. Croat, and K. F. Kelton, The effect of phase separation on subsequent crystallization in $Al_{88}Gd_6La_2Ni_4$, Acta Mater. **48**, 4035 (2000).
[47] K. F. Kelton, T. K. Croat, A. K. Gangopadhyay, L. Q. Xing, A. L. Greer, M. Weyland, X. Li, and K. Rajan, Mechanisms for nanocrystal formation in metallic glasses, J. Non Cryst. Solids **317**, 71 (2003).
[48] M. D. H. Lay, A. J. Hill, P. G. Saksida, M. A. Gibson, and T. J. Bastow, ^{27}Al NMR measurement of fcc Al configurations in as-quenched $Al_{85}Ni_{11}Y_4$ metallic glass and crystallization kinetics of Al nanocrystals, Acta Mater. **60**, 79 (2012).
[49] J. Antonowicz, Atomic packing and phase separation in Al-rare earth metallic glasses, J. Mater. Sci. **45**, 5040 (2010).
[50] J. Bokeloh, N. Boucharat, H. Rösner, and G. Wilde, Primary crystallization in Al-rich metallic glasses at unusually low temperatures, Acta Mater. **58**, 3919 (2010).
[51] Q. Li, E. Johnson, M. B. Madsen, A. Johansen, and L. Sarholt-Kristensen, Crystallization of Al-based metallic glasses. Structural aspects, Philos. Mag. B **66**, 427 (1992).
[52] G. Wilde, N. Boucharat, R. J. Hebert, H. Rösner, W. S. Tong, and J. H. Perepezko, Nanocrystallization in Al-rich Metallic Glasses, Adv. Eng. Mater. **5**, 125 (2003).
[53] S. Plimpton, Fast parallel algorithms for short-range molecular dynamics, J. Comput. Phys. **117**, 1 (1995).
[54] Y. Q. Cheng, E. Ma, and H. W. Sheng, Atomic Level Structure in Multicomponent Bulk Metallic Glass, Phys. Rev. Lett. **102**, 245501 (2009).
[55] Y. Y. Cui, T. L. Wang, J. H. Li, Y. Dai, and B. X. Liu, Thermodynamic calculation and interatomic potential to predict the favored composition region for the Cu–Zr–Al metallic glass formation, PCCP **13**, 4103 (2011).
[56] X. Liu, E. Luber, D. Mitlin, and H. Zhang, Design of high Tg Zr-based metallic glasses using atomistic simulation and experiment, Philos. Mag. **91**, 3393 (2011).
[57] P. J. Steinhardt, D. R. Nelson, and M. Ronchetti, Bond-orientational order in liquids and glasses, Phys. Rev. B **28**, 784 (1983).
[58] S. Winczewski, J. Dziedzic, and J. Rybicki, A highly-efficient technique for evaluating bond-orientational order parameters, Comput. Phys. Commun. **198**, 128 (2016).
[59] W. Mickel, S. C. Kapfer, G. E. Schröder-Turk, and K. Mecke, Shortcomings of the bond orientational order parameters for the analysis of disordered particulate matter, J. Chem. Phys. **138**, 044501 (2013).
[60] P. Egelstaff, *An Introduction to the Liquid State* (Elsevier Science, Amsterdam, 2012).
[61] R. Böhmer, K. L. Ngai, C. A. Angell, and D. J. Plazek, Non-exponential relaxations in strong and fragile glass formers, J. Chem. Phys. **99**, 4201 (1993).
[62] J. Han, W. Y. Wang, C. Wang, Y. Wang, X. Liu, and Z.-K. Liu, Accurate determination of thermodynamic properties for liquid alloys based on *ab initio* molecular dynamics simulation, Fluid Phase Equilib. **360**, 44 (2013).

[63] S.-T. Lin, M. Blanco, and W. A. G. III, The two-phase model for calculating thermodynamic properties of liquids from molecular dynamics: Validation for the phase diagram of Lennard-Jones fluids, J. Chem. Phys. **119**, 11792 (2003).

[64] Q. Jing-Yu, A new model for the configurational entropy of mixing in liquid alloys based on short-range order, Acta Phys. Chim. Sin. **28**, 1586 (2012).

[65] A. B. Bhatia and D. E. Thornton, Structural aspects of the electrical resistivity of binary alloys, Phys. Rev. B **2**, 3004 (1970).

[66] K. A. Jackson, The interface kinetics of crystal growth processes, Interface Sci. **10**, 159 (2002).

[67] J. W. P. Schmelzer, R. Müller, J. Möller, and I. S. Gutzow, Theory of nucleation in viscoelastic media: Application to phase formation in glass-forming melts, J. Non Cryst. Solids **315**, 144 (2003).

[68] See Supplemental Material at http://link.aps.org/supplemental/10.1103/PhysRevMaterials.4.093608 for an extended result of the structural transition, kinetic properties and thermodynamic signal upon rapid cooling of $AlZr_3$, Al_3Zr_5, Al_4Zr_5, and Al_3Zr, respectively. The atomic structure evolution in the supercooled liquid of $AlZr_3$, Al_3Zr_5, and Al_4Zr_5 are given for comparison.

[69] M. D. Ediger, C. A. Angell, and S. R. Nagel, Supercooled liquids and glasses, J. Phys. Chem. **100**, 13200 (1996).

[70] W. Götze, Recent tests of the mode-coupling theory for glassy dynamics, J. Phys.: Condens. Matter **11**, A1 (1999).

[71] I. Chang and H. Sillescu, Heterogeneity at the glass transition: Translational and rotational self-diffusion, J. Phys. Chem. B **101**, 8794 (1997).

[72] T. Kawasaki and A. Onuki, Slow relaxations and stringlike jump motions in fragile glass-forming liquids: Breakdown of the Stokes-Einstein relation, Phys. Rev. E **87**, 012312 (2013).

[73] X. P. Tang, U. Geyer, R. Busch, W. L. Johnson, and Y. Wu, Diffusion mechanisms in metallic supercooled liquids and glasses, Nature **402**, 160 (1999).

[74] C. A. Angell, K. L. Ngai, G. B. McKenna, P. F. McMillan, and S. W. Martin, Relaxation in glass-forming liquids and amorphous solids, J. Appl. Phys. **88**, 3113 (2000).

[75] D. Huang and G. B. McKenna, New insights into the fragility dilemma in liquids, J. Chem. Phys. **114**, 5621 (2001).

[76] B. J. Gellatly and J. L. Finney, Characterisation of models of multicomponent amorphous metals: The radical alternative to the Voronoi polyhedron, J. Non Cryst. Solids **50**, 313 (1982).

[77] J. L. Finney, Modelling the structures of amorphous metals and alloys, Nature **266**, 309 (1977).

[78] H. W. Sheng, W. K. Luo, F. M. Alamgir, J. M. Bai, and E. Ma, Atomic packing and short-to-medium-range order in metallic glasses, Nature **439**, 419 (2006).

[79] Y. B. Wang, H. W. Yang, B. B. Sun, B. Wu, J. Q. Wang, M. L. Sui, and E. Ma, Evidence of phase separation correlated with nanocrystallization in $Al_{85}Ni_5Y_6Fe_2Co_2$ metallic glass, Scr. Mater. **55**, 469 (2006).

[80] Y. E. Kalay, I. Kalay, J. Hwang, P. M. Voyles, and M. J. Kramer, Local chemical and topological order in Al–Tb and its role in controlling nanocrystal formation, Acta Mater. **60**, 994 (2012).

[81] Y. Xie, S. Sohn, J. Schroers, and J. J. Cha, Direct observation through *in situ* transmission electron microscope of early states of crystallization in nanoscale metallic glasses, JOM **69**, 2187 (2017).

[82] J. Han, C. Wang, X. Liu, Y. Wang, Z.-K. Liu, and J. Jiang, Atomic-level mechanisms of nucleation of pure liquid metals during rapid cooling, Chem. Phys. Chem. **16**, 3916 (2015).

[83] K. Nishio, A. K. A. Lu, and T. Miyazaki, Universal short-range order and material dependent glass-forming ability of metallic liquids and glasses, Phys. Rev. Res. **1**, 012013 (2019).

[84] S. Tang, J. C. Wang, B. Svendsen, and D. Raabe, Competitive bcc and fcc crystal nucleation from non-equilibrium liquids studied by phase-field crystal simulation, Acta Mater. **139**, 196 (2017).

[85] Y. Xie, S. Sohn, M. Wang, H. Xin, Y. Jung, M. D. Shattuck, C. S. O'Hern, J. Schroers, and J. J. Cha, Supercluster-coupled crystal growth in metallic glass forming liquids, Nat. Commun. **10**, 915 (2019).

[86] Y. Shibuta, S. Sakane, E. Miyoshi, S. Okita, T. Takaki, and M. Ohno, Heterogeneity in homogeneous nucleation from billion-atom molecular dynamics simulation of solidification of pure metal, Nat. Commun. **8**, 10 (2017).

[87] G. Kurtuldu, A. Sicco, and M. Rappaz, Icosahedral quasicrystal-enhanced nucleation of the fcc phase in liquid gold alloys, Acta Mater. **70**, 240 (2014).

[88] G. Kurtuldu, P. Jarry, and M. Rappaz, Influence of Cr on the nucleation of primary Al and formation of twinned dendrites in Al–Zn–Cr alloys: Can icosahedral solid clusters play a role? Acta Mater. **61**, 7098 (2013).

[89] J. Schroers, Glasses made from pure metals, Nature **512**, 142 (2014).

[90] M. Blank-Bewersdorff, Crystallization behaviour of $Al_{86}Ni_{10}Zr_4$ and $Al_{86}Fe_{10}Zr_4$ metallic glasses, J. Mater. Sci. Lett. **10**, 1225 (1991).

[91] J. C. Foley, D. R. Allen, and J. H. Perepezko, Analysis of nanocrystal development in Al-Y-Fe and Al-Sm glasses, Scr. Mater. **35**, 655 (1996).

[92] P. Ganesh and M. Widom, *Ab initio* simulations of geometrical frustration in supercooled liquid Fe and Fe-based metallic glass, Phys. Rev. B **77**, 014205 (2008).